

Discovery of an Edge-on Circumstellar Debris Disk around BD+45° 598: A Newly Identified Member of the β Pictoris Moving Group

```
Sasha Hinkley<sup>1</sup>, Elisabeth C. Matthews<sup>2</sup>, Charlène Lefevre<sup>3</sup>, Jean-Francois Lestrade<sup>4</sup>, Grant Kennedy<sup>5</sup>,
Dimitri Mawet<sup>6,7</sup>, Karl R. Stapelfeldt<sup>7</sup>, Shrishmoy Ray<sup>1</sup>, Eric Mamajek<sup>7</sup>, Brendan P. Bowler<sup>8</sup>, David Wilner<sup>9</sup>, Jonathan Williams<sup>10</sup>, Megan Ansdell<sup>10,11</sup>, Mark Wyatt<sup>12</sup>, Alexis Lau<sup>13</sup>, Mark W. Phillips<sup>1</sup>, Jorge Fernandez Fernandez<sup>5</sup>, Jonathan Gagné<sup>14,15</sup>, Emma Bubb<sup>16</sup>, Ben J. Sutlieff<sup>17,18</sup>, Thomas J. G. Wilson<sup>1</sup>, Brenda Matthews<sup>19,20</sup>, Henry Ngo<sup>19</sup>,
                      Danielle Piskorz<sup>7</sup>, Justin R. Crepp<sup>21</sup>, Erica Gonzalez<sup>21</sup>, Andrew W. Mann<sup>22</sup>, and Gregory Mace<sup>8</sup> 

<sup>1</sup> University of Exeter, Astrophysics Group, Physics Building, Stocker Road, Exeter EX4 4QL, UK

<sup>2</sup> l'Observatoire Astronomique de IUniversité de Genève, Versoix, Switzerland
                                   <sup>3</sup> Institut de RadioAstronomie Millimétrique (IRAM), 300 rue de la Piscine, F-38406 Saint Martin dHères, France
                 <sup>4</sup> LERMA, Observatoire de Paris, PSL Research University, CNRS, Sorbonne Universités, UPMC Univ. Paris 06, F-75014 Paris, France
                                                                 Department of Physics, University of Warwick, Coventry CV4 7AL, UK
             <sup>6</sup> Department of Astronomy, California Institute of Technology, Mail Code 249-17, 1200 E. California Boulevard, Pasadena, CA 91125, USA
                       Jet Propulsion Laboratory, California Institute of Technology, M/S 321-100, 4800 Oak Grove Drive, Pasadena, CA 91109, USA

Department of Astronomy, The University of Texas at Austin, 2515 Speedway Boulevard Stop C1400, Austin, TX 78712, USA
                                        Center for Astrophysics | Harvard & Smithsonian, 60 Garden Street, MS 42, Cambridge, MA 02138, USA

10 Institute for Astronomy, 2680 Woodlawn Drive, Honolulu, HI 96822-1897, USA
                                                                    NASA Headquarters, 300 E Street SW, Washington, DC 20546, USA
                                              12 Institute of Astronomy, University of Cambridge, Madingley Road, Cambridge CB3 0HA, UK
                                                                           Aix Marseille Univ, CNRS, CNES, LAM, Marseille, France
                                 <sup>14</sup> Planétarium Rio Tinto Alcan, Espace pour la vie, 4801 av. Pierre-De Coubertin, Montréal, QC H1V 3V4, Canada
      <sup>15</sup> Institute for Research on Exoplanets, Université de Montréal, Département de Physique, C.P. 6128 Succ. Centre-ville, Montréal, QC H3C 3J7, Canada <sup>16</sup> Institute for Astronomy, The University of Edinburgh, Royal Observatory, Blackford Hill, Edinburgh EH9 3HJ UK
                      Anton Pannekoek Institute for Astronomy, University of Amsterdam, Science Park 904, 1098 XH Amsterdam, The Netherlands Leiden Observatory, Leiden University, P.O. Box 9513, 2300 RA Leiden, The Netherlands
     <sup>19</sup> Herzberg Astronomy & Astrophysics Research Centre, National Research Council of Canada, 5071 West Saanich Road, Victoria, BC V9E 2E7, Canada
                                   Department of Physics & Astronomy, University of Victoria, 3800 Finnerty Road, Victoria, BC V8P 5C2, Canada <sup>21</sup> Department of Physics, University of Notre Dame, 225 Nieuwland Science Hall, Notre Dame, IN 46556, USA
        <sup>22</sup> University of North Carolina, Department of Physics & Astronomy, 120 E. Cameron Avenue, Phillips Hall CB3255, Chapel Hill, NC 27599, USA
                                            Received 2020 December 9; revised 2021 March 2; accepted 2021 March 4; published 2021 May 11
```

Abstract

We report the discovery of a circumstellar debris disk viewed nearly edge-on and associated with the young, K1 star BD+45° 598 using high-contrast imaging at 2.2 μ m obtained at the W.M. Keck Observatory. We detect the disk in scattered light with a peak significance of ~5 σ over three epochs, and our best-fit model of the disk is an almost edge-on ~70 au ring, with inclination angle ~87°. Using the NOEMA interferometer at the Plateau de Bure Observatory operating at 1.3 mm, we find resolved continuum emission aligned with the ring structure seen in the 2.2 μ m images. We estimate a fractional infrared luminosity of $L_{\rm IR}/L_{\rm tot} \simeq 6^{+2}_{-1} \times 10^{-4}$, higher than that of the debris disk around AU Mic. Several characteristics of BD+45° 598, such as its galactic space motion, placement in a color–magnitude diagram, and strong presence of lithium, are all consistent with its membership in the β Pictoris Moving Group with an age of 23 \pm 3 Myr. However, the galactic position for BD+45° 598 is slightly discrepant from previously known members of the β Pictoris Moving Group, possibly indicating an extension of members of this moving group to distances of at least 70 pc. BD+45° 598 appears to be an example from a population of young circumstellar debris systems associated with newly identified members of young moving groups that can be imaged in scattered light, key objects for mapping out the early evolution of planetary systems from ~10–100 Myr. This target will also be ideal for northern-hemisphere, high-contrast imaging platforms to search for self-luminous, planetary mass companions residing in this system.

Unified Astronomy Thesaurus concepts: Circumstellar disks (235)

1. Introduction

Circumstellar debris disks are composed of the rocky or icy planetesimal bodies created in the planet formation process, as well as the tenuous dust and gas generated by their ongoing collisions (e.g., Wyatt 2008; Matthews et al. 2014; Hughes et al. 2018). The dust in debris disk systems, the presence of which is usually detected by excess far-infrared emission above the stellar photosphere (e.g., Aumann et al. 1984), is inherently short-lived, as the small released particles should be removed either by radiative forces, or accretion inwards by Poynting–Robertson drag (Backman & Paresce 1991; Dominik &

Decin 2003; Kenyon & Bromley 2004). The long-term presence of dust in these systems thus suggests that it is being replenished by the continuous fragmentation of the parent planetesimals, which have been excited to eccentric orbits, causing them to experience ongoing collisions (e.g., Wyatt & Dent 2002; Rieke et al. 2005). This planetesimal fragmentation can be driven by several physical mechanisms, including perturbations by the most massive planetesimals (Kenyon & Bromley 2008; Pan & Schlichting 2012), or a planetary mass companion embedded within or exterior to the disk (Kenyon & Bromley 2004; Wyatt 2005; Mustill & Wyatt 2009). Thus, in addition to identifying themselves as a site of efficient

planetesimal formation, stars with large amounts of circumstellar dust may be more likely to host massive planets at wide orbital separations (e.g., Mouillet et al. 1997; Augereau et al. 2001) suitable for direct imaging. However, no significant correlation between debris disk brightness and planets identified by any discovery method has yet been found (Bryden et al. 2009; Moro-Martín et al. 2015; Meshkat et al. 2017; Yelverton & Kennedy 2018).

Surveys carried out by space-based observatories such as Spitzer, Herschel, and WISE have uncovered hundreds of stars within $\sim 200 \,\mathrm{pc}$ with a significant infrared excess in their spectral energy distributions at 22–24 µm suggesting the presence of warm circumstellar dust (e.g., Trilling et al. 2008; Carpenter et al. 2009; Cotten & Song 2016; Patel et al. 2017; Silverberg et al. 2018), or a colder component identified by an excess at 70–160 μ m (e.g., Hillenbrand et al. 2008; Matthews et al. 2010; Eiroa et al. 2013; Sibthorpe et al. 2018). The identification of these circumstellar disks has also coincided with several high-contrast imaging surveys targeting stars with an infrared excess (e.g., Janson et al. 2013; Rameau et al. 2013; Nielsen et al. 2019; Launhardt et al. 2020). Scattered-light images of debris disk systems in the optical or near-infrared ($\lesssim 2 \,\mu \text{m}$) returned by these surveys (e.g., Esposito et al. 2020) are particularly powerful for characterizing planetary systems, as the morphology of stable debris belts may reveal the gravitational influence of giant planets sculpting the dust distribution through resonant interactions (e.g., Wyatt 2003; Chiang et al. 2009; Morales et al. 2011; Su et al. 2013; Matthews et al. 2018). When combined with a flux density distribution (or spectral energy distribution, SED) of the system with adequate wavelength coverage, the spatial distribution of the dust structure can also provide constraints on the dust grain composition and size distribution.

To characterize planetary systems at the earliest stages, and specifically to identify where planets reside shortly after the epoch of planet formation has ended, the youngest debris systems are particularly important. The nearest OB Associations (e.g., the Scorpius-Centaurus Association, ~10-20 Myr, Pecaut et al. 2012) have provided numerous scattered light images of young debris disks (e.g., Matthews et al. 2017; Bonnefoy et al. 2017; Esposito et al. 2020). However, these associations are inherently at greater distances (\sim 140 pc), limiting the achievable physical resolution of 8-10 m telescopes. The best compromise offering close proximity $(\sim 20-60 \,\mathrm{pc})$ and relative youth $(\sim 10-100 \,\mathrm{Myr})$ are therefore nearby Young Moving Groups (YMGs; Torres et al. 2006; Bell et al. 2015; Gagné et al. 2018): loose associations of gravitationally unbound stars sharing similar galactic space motions. Indeed, early discoveries of debris disks around YMG members have been extremely important for the development of our understanding of planetary systems (Smith & Terrile 1984; Rebull et al. 2008; Donaldson et al. 2012; Riviere-Marichalar et al. 2014; Moór et al. 2016). The latertype members (spectral types K and later) of YMGs should form the majority of the population of these groups, but have only begun to be identified in large numbers in the last several years, partly with the arrival of kinematic data from the Gaia mission (e.g., Kraus et al. 2014; Gaia Collaboration et al. 2018; Gagné & Faherty 2018; Bowler et al. 2019). However, \sim 90% of all debris disks²³ imaged in scattered light are associated

with spectral types earlier than K, due to observational limitations, or the higher surface brightness of disks associated with early-type stars that have higher luminosity. Therefore, late-type members of nearby YMGs may represent the best opportunity to identify a yet undiscovered population of young debris disks, key pieces in our process of mapping out the evolution of planetary systems from ${\sim}10$ to $100\,\mathrm{Myr}.$

BD+45° 598 (2MASS J02211307+4600070, TYC 3294-2222-1) is a young, active, Li-rich K1-type star at 73.180 ± 0.123 pc (Gaia Collaboration et al. 2021)²⁴ that was first characterized in a spectroscopic survey of ROSAT All-Sky Survey (RASS) X-ray sources by Guillout et al. (2009), and later flagged by Moór et al. (2011) as a possible member of the β Pictoris Moving Group (BPMG, hereafter). Based on its $22 \,\mu \text{m}$ excess, BD+ 45° 598 was also identified in Cotten & Song (2016) as one of their "reserve" IR excess stars, reporting a $L_{\rm IR}/L_{\rm star}=3.9\times10^{-4}$, and a dust temperature of 240 K. Note, however, that Cotten & Song (2016) report an excess only in the 22 μ m band, and the temperature and luminosity of a two-parameter blackbody cannot be constrained by a single data point. The WISE emission could therefore arise from a more luminous dust population that resides much farther from the star and at a much cooler temperature.

In this paper, we report the discovery of an edge-on debris ring associated with BD+45° 598 obtained using high-contrast imaging at the W.M. Keck Observatory (Figure 1). The clear signatures of youth and K1 spectral type make it a valuable object for the characterization of the early evolution of planetary systems surrounding late-type stars, similar to our own solar system. In Section 2 we give an overview of our near-IR and millimeter observations and data processing, and in Section 3 we describe our model fitting process to both the infrared scattered light and millimeter images of the ring. In Section 4, we show that this object is a likely member of the BPMG, and we summarize in Section 5.

2. Observations and Data Post-processing

Below we describe our observational coverage of BD +45° 598 at the W.M. Keck Observatory, the James Clerk Maxwell Telescope (JCMT), Submillimeter Array (SMA), the Institut de RadioAstronomie Millimétrique (IRAM), and the Immersion Grating INfrared Spectrometer (IGRINS) at McDonald Observatory.

2.1. Scattered Light Observations at the W.M. Keck Observatory

Table 1 provides the detailed parameters of our observations of BD+45° 598, which was first observed on UT 2013 September 25 with the NIRC2 instrument at the W.M. Keck Observatory using the K' filter (2.124 μ m central wavelength) and the 400 milliarcsecond coronagraphic mask. The two subsequent epochs of observation of BD+45° 598 were obtained using this mask, and the 200 milliarcsecond radius of this mask effectively sets the ultimate inner working angle for our observations. Seeing measurements obtained at Keck indicate that the average 0.5 μ m seeing for the 2013 and 2014 epochs ranged from 0."5 to 0."6, but was poorer (~0."8) for the 2015 epoch. All scattered light observations were obtained

²³ Data obtained from webdisks.jpl.nasa.gov, accessed on 2020 May 18.

 $[\]overline{^{24}}$ Distance calculated as $D=1/\varpi$ with $\varpi=13.6480\pm0.0230$ mas from Gaia Collaboration et al. (2021), corrected by -0.017 mas following Lindegren et al. (2021).

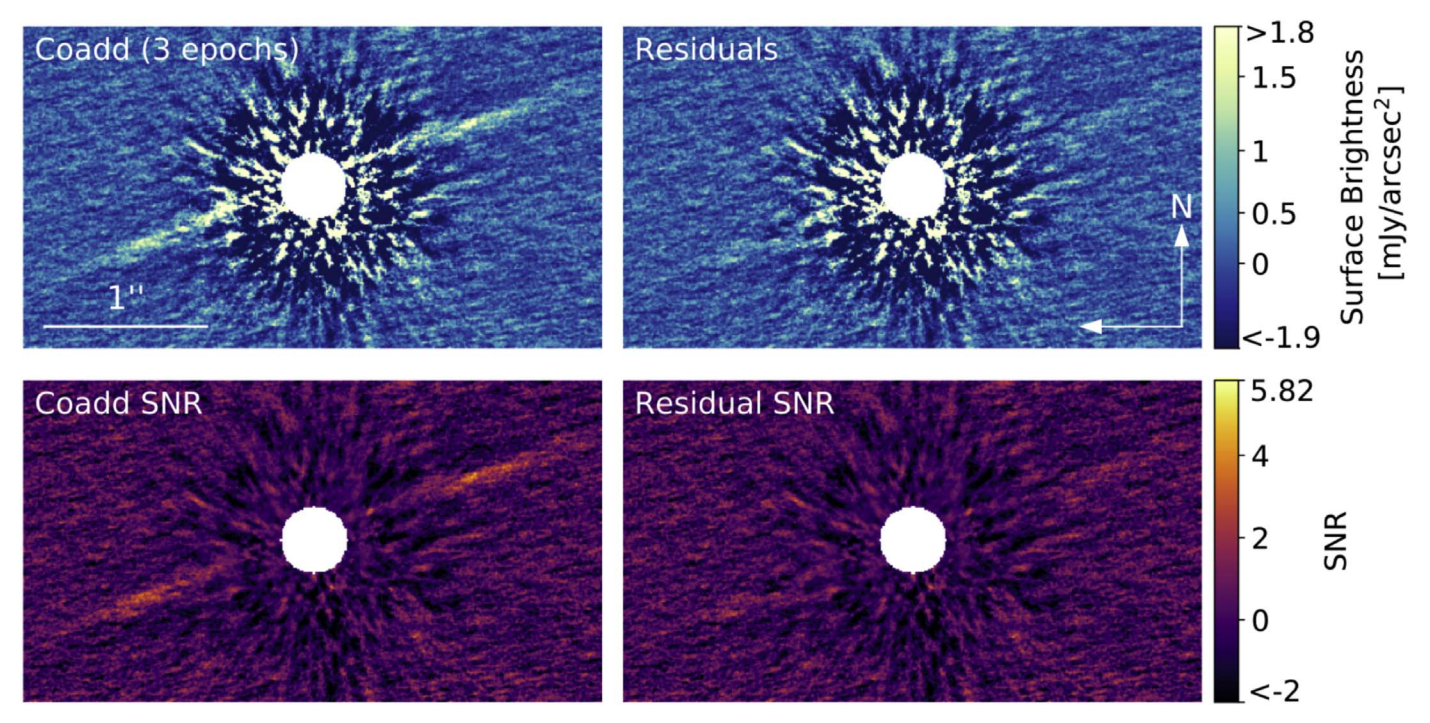


Figure 1. Top row: coadded $2.2 \mu m$ data for the three high-quality epochs (top left), and the coadded residual map with the best-fitting model subtracted from each epoch (top right). The weighted average of the three models presented in Table 1 has been subtracted from the cleaned data, which is then processed using the KLIP algorithm. While some of the stellar speckles are saturated in this image, the full dynamic range of the disk signal is displayed. Bottom row: signal-to-noise maps of the coadded image and the residual image. The disk is detected at lower significance at very small separations from the star, due to the higher level of residual scattered starlight, as well as self-subtraction due to the KLIP algorithm. In the residual images, a faint signal can be seen along the plane of the disk at low significance. The top images are scaled with the square of the intensity, while the bottom images are scaled linearly.

using the Keck Adaptive Optics ("AO") system (Wizinowich et al. 2000), operating in pupil tracking mode (Marois et al. 2006), to differentiate quasi-static speckles (e.g., Hinkley et al. 2007) from any bona fide astrophysical sources. To remove the residual, uncorrected starlight, we model this speckle pattern using a customized algorithm based on projections of the data onto Karhunen–Loève eigenimages (the Karhunen–Loève Image Processing or "KLIP" algorithm, Soummer et al. 2012). Subtracting this model from each image provides deep contrast relative to the host star. However, because of the \sim 46° decl. of BD+45° 598, Table 1 shows that typically only 18°–36° of parallactic angle rotation could be achieved for each of our three epochs of scattered light imaging, meaning a substantial amount of residual scattered starlight contamination remains within \sim 0".5.

In Figure 2 we show an image of BD+45° 598 with our three epochs of data coadded together, as well as a corresponding signal-to-noise (S/N) map of the same image. The disk was immediately identified in our first epoch (Figure 2, top panels), extending to $\sim 1''$ on each side of the star. The disk structure in the images was robust against the number of eigenmodes chosen in the post-processing algorithm, further indicating that the structure is a true astrophysical signal, and not residual, scattered starlight. However, to verify that the signal was indeed a physical structure associated with the star, BD $+45^{\circ}$ 598 was again detected using the K' filter at two subsequent epochs, 2014 October 2 and 2015 January 10 (see Figure 2). We also attempted another observation of BD +45° 598 on 2014 November 11, but this data set suffered from poor atmospheric conditions corresponding to poor Adaptive Optics correction, resulting in a nondetection of the disk.

2.2. JCMT and SMA

BD+45° 598 was not observed by either the Spitzer or Herschel observatories, and there are only upper limits available at 60 μ m and 100 μ m from IRAS. So, as an additional check that this structure seen in the Keck images was not an artifact from the image post-processing, BD+45° 598 was observed at various dates between 2016 February 19 and 2016 August 10 for a total of 4.5 hr at 850 μ m (Band 3) using the SCUBA-2 instrument at the James Clerk Maxwell Telescope. The SCUBA-2 observations achieved an rms sensitivity of 1.1 mJy per 14.5 arcsecond beam, but no signal at the location of BD+45° 598 was detected. These observations thus provide an upper limit of 3.3 mJy at 850 μ m, and we do not include these limits for our analysis. Using the Submillimeter Array (SMA) on 2015 August 10, we observed BD+45° 598 at 224 GHz (1.3 mm) in a six hour "filler track." The array configuration using six antennas resulted in a 5.0×2.7 beam, and using a point-source fit to the imaged visibilities, our observations revealed a $\sim 3.3\sigma$ detection of a source with a flux density of 2.17 ± 0.76 mJy, coincident with the location of the disk seen in scattered light. The observations followed standard procedures, with 3c84 and 0303+472 used as gain calibrators, and Uranus as the flux calibrator.

2.3. IRAM

With the goal of obtaining better resolution on the unresolved SMA detection, we observed the field around BD +45° 598 at 230.5 GHz during the winter periods in 2015–16 and 2016–17 using seven antennae with the IRAM NOEMA interferometer at Plateau de Bure at an altitude of 2552 meters. The first session used the compact BD array configuration, with

Table 1Imaging Observations for BD+45° 598

Date (UT)	Observatory/Instrument	Wavelength/Mode	Integration Time	Notes
Scattered light imaging				
2013 Sep 25	WMKO/NIRC2	$2.2~\mu m$ coronagraphy	$50 \times 30 \text{ s} = 1500 \text{ s}$	parallactic angle rotation = 17.8
2014 Oct 2		$2.2 \ \mu m$ coronagraphy	$130 \times 20 \text{ s} = 2600 \text{ s}$	parallactic angle rotation = $36^{\circ}0$
2015 Jan 10		2.2 μ m coronagraphy	$64 \times 24 \text{ s} = 1536 \text{ s}$	parallactic angle rotation = $20^{\circ}6$
1.3 mm imaging				
Various	JCMT/SCUBA-2	850 μ m imaging	4.2 hr	
2015 Aug 10	SMA	224 GHz imaging	6.0 hr	Filler Observation
2015 Nov 27	IRAM/NOEMA	230.5 GHz imaging	2.1 hr	CD configuration, resolution: 2"
2015 Dec 2			1.1 hr	CD configuration, resolution: 2"
2017 Jan 3	•••	•••	6.4 hr	AZ configuration, resolution: 0"5

projected baseline lengths <200 m on 2015 November 27 (2.1 hr) and 2015 December 02 (1.1 hr), the second session used the extended A array configuration, with projected baseline lengths up to 800 m on 2017 January 3 (6.4 hr). All observations were conducted during fair weather conditions (precipitable water vapor \sim 2–3 mm) apart from those on 2015 December 2, which were not used in our data processing. The data were processed with the Widex correlator over a bandwidth of 3.6 GHz centered on 230.5 GHz in both polarizations combined to provide total intensity visibilities. Phase calibrators J0136+478 and J0300+470 were used to monitor the atmospheric phase variations once every 30 minutes to remove its effect on the target phase. Absolute flux density calibration relies on the monitoring program of standard calibrators (MWC 349 and LkHa 101) conducted routinely by IRAM. At 1.3 mm, the flux density uncertainty can be up to 20%.

The NOEMA data were processed with the IRAM software GILDAS. The data acquired at the three epochs of observations were combined to provide satisfactory uv-coverage. Measured complex visibilities were Fourier inverted and deconvolved using the CLEAN algorithm (Högbom 1974) to provide the final intensity map shown in Figure 3. The data processing used natural cleaning with an elliptical support large enough to include the source and keep some sidelobes (5" by 10" with a position angle close to the disk orientation in the Keck image). One thousand iterations were carried out, but the convergence of the flux density was satisfactorily reached after a few hundred. The image has a beam size of (0."68 \times 0."52) and is limited in extent by the primary beam of individual antennas (18" at 230 GHz).

In the CLEAN map shown in Figure 3, we find a millimeterwavelength structure detected with a statistical significance of 4σ – 5σ , elongated and aligned with the edge-on disk seen in the Keck image (see discussion of the NOEMA data modeling in Section 3.2). The NOEMA structure is well centered at the optical position of BD+45° 598 provided by the Gaia DR2 catalog (Gaia Collaboration et al. 2018) updated with its proper the observation midpoint at $(\alpha = 02^{\text{h}}21^{\text{m}}13.15055 \pm 0.00013)$ and $\delta = +46^{\circ}00'06.''4333 \pm 0.''0011$ at 2016.0). The Gaia and NOEMA celestial reference frames are aligned at the submilliarcsecond level (Lindegren 2020).

The elongated NOEMA structure in the map of Figure 3 is almost certainly millimeter-sized dust that traces a belt of planetesimals centered on BD+45° 598 corresponding to the Keck scattered light images. We note that the west side of the structure is more prominent than the east side, but our modeling finds that any brightness asymmetry is only at the $\sim 2\sigma$ level.

The integrated flux density of the disk at $\lambda = 1.3 \, \mathrm{mm}$ is $1.11 \pm 0.17 \, \mathrm{mJy}$ (statistical uncertainty). This measurement was done by fitting an ellipsoid to the data in the *uv*-plane with a priori values conjectured from the image itself. The photospheric flux density of BD+45° 598 is three orders of magnitude smaller at this wavelength and so does not contribute. Finally, using the beam full width at half maximum combined with the distance to BD+45° 598, we can infer that the belt width is smaller than 35 au.

2.4. IGRINS

For the purpose of kinematic analysis, we obtained an improved radial velocity of the star by observing with the IGRINS spectrograph (Park et al. 2014) at the McDonald Observatory on 2015 October 23. A total exposure time of 360 s was obtained in the "ABBA" observing pattern, and 200 s were obtained for the purpose of telluric calibration on the star HD14212. Cross-correlation against other objects with similar spectral types provides an absolute radial velocity of $0.18\pm0.22~{\rm km~s}^{-1}.$

3. Results and Model Fitting

Below we describe the result of our modeling of the $2.2 \,\mu\text{m}$ Keck scattered light images, as well as the IRAM interferometric imaging at 1.3mm.

3.1. Coronagraphic K'-band Scattered Light Imaging

Our K'-band coronagraphic images are presented in Figure 2 for the three epochs where we model the disk geometry. No disk signal was detected during our 2014 November 11 observations, and so we do not model these data. For the three epochs shown in Figure 2, we detect a peak S/N for the disk of 4.8, 4.8, and 4.7, respectively. The bottom panel of Figure 1 also shows an S/N map for the combined data set, indicating a peak S/N of 5.8. Figure 1 (top panel) also shows a measure of the disk surface brightness, indicating a peak surface brightness of $\sim 1-2$ mJy arcsec $^{-2}$. However, it should be noted that in the speckle dominated regime at inner working angles $\lesssim 0.995$, some "self-subtraction" due to the KLIP algorithm will diminish the surface brightness of the disk by a factor of ~ 2 .

To constrain the disk geometry, we use an injection modeling process as described in Wahhaj et al. (2014) and Matthews et al. (2017). We fit a circular disk with five free parameters to the data. These parameters are the position angle, inclination angle, disk radius, forward scattering (parameterized by the Henyey–Greenstein parameter g), and an overall

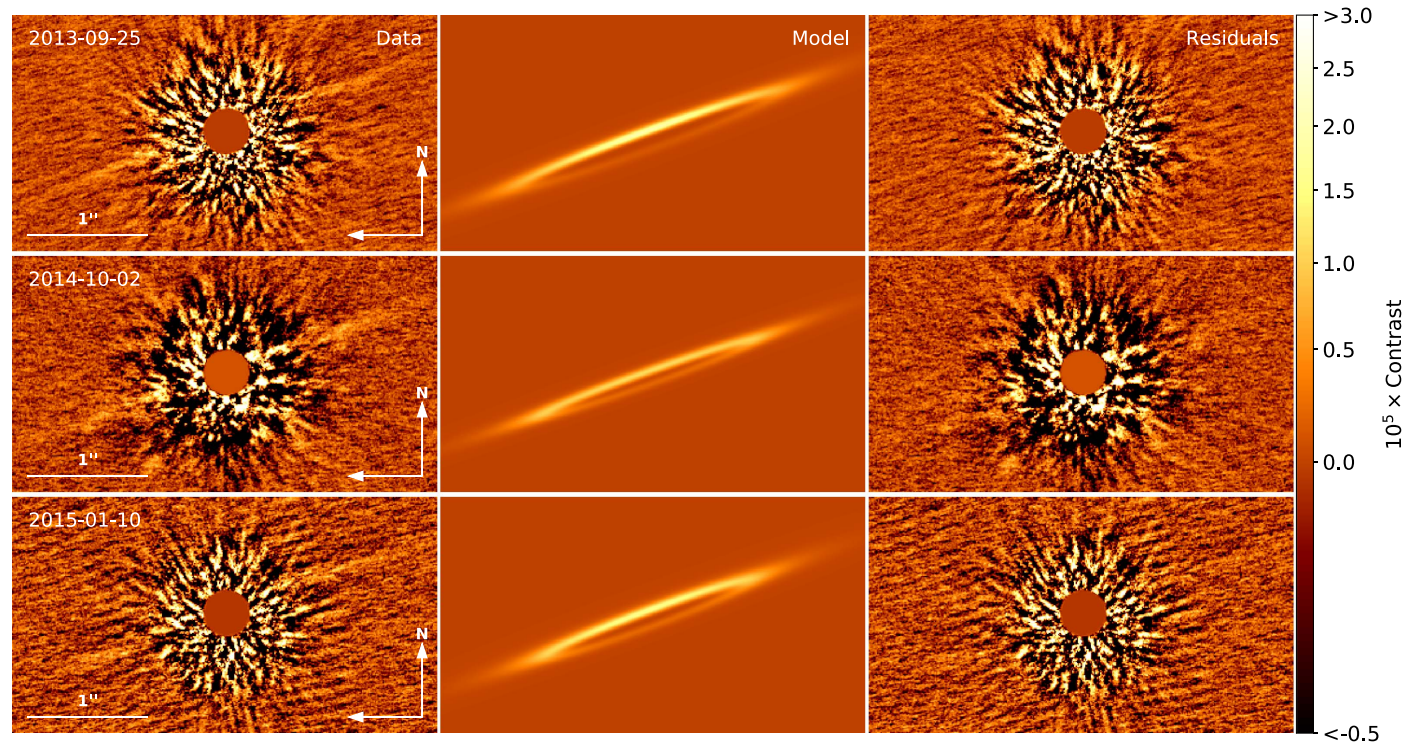


Figure 2. Processed 2.2 μ m data (left column) and best-fitting models (middle) with corresponding residuals (right) for the three Keck/NIRC2 epochs in which the debris disk was detected. Full details of the fitting process and derived values are included in Section 3.

scaling term. Synthetic model images of an optically thin ring are generated using the GRaTeR radiative transfer code (Augereau et al. 1999), and then convolved with a Gaussian function to reproduce the resolution of the telescope. To generate disk models with GRaTeR, we use the following parameterization. The disk density is calculated as

$$\rho = \frac{\rho_{\rm o} \exp\left(\left[\frac{-|z|}{\xi_{\rm o}} \left(\frac{r}{r_{\rm o}}\right)^{-\beta}\right]^{\gamma}\right)}{\sqrt{\left(\frac{r}{r_{\rm o}}\right)^{-2\alpha_{\rm in}} + \left(\frac{r}{r_{\rm o}}\right)^{-2\alpha_{\rm out}}}},\tag{1}$$

where r is the radial distance from the disk center, z is the vertical distance from the disk midplane, and the remaining terms are parameters defining the disk vertical and radial structure. For this work, the only disk parameters we fit are ρ_0 and r_0 ; values for the other parameters are fixed at $\alpha_{in} = 10$, $\alpha_{out} = -3$, $\xi_0 = 1$, $\beta = 0$, and $\gamma = 2$, i.e., we fit a thin, narrow ring and do not attempt to constrain the vertical disk structure since this is unresolved in the Keck/NIRC2 data.

The scattered light contribution from each point in the disk is calculated as:

$$F \propto \frac{\rho \times p(\theta)}{d^2},\tag{2}$$

where θ is the scattering angle of the dust, and d is the distance from the star to each point, and $p(\theta)$ is the scattering phase function. In each fit, the disk is scaled by an arbitrary value ρ_0 , which takes into account the effect of various factors including the stellar luminosity, stellar distance, and telescope gain. For

 $p(\theta)$ we use the Henyey–Greenstein scattering function:

$$p(\theta) = \frac{1}{4\pi} \frac{1 - g^2}{[1 - 2g\cos\theta + g^2]^{\frac{3}{2}}}.$$
 (3)

This calculation is performed over a grid encompassing the entire disk, and contributions along each line of sight are added to create a final disk image. As well as the ρ_0 , r_0 , and g disk parameters, we fit two geometrical viewing terms, namely the position angle and the inclination of the disk, denoted by PA and i_{tilt} .

These models are then rotated and subtracted from each individual data frame in the cleaned data cubes. These data cubes with negative disks injected are processed using the same KLIP algorithm discussed in Section 2.1. By injecting negative disk images into the cleaned data, we mimic a forward-modeling procedure whereby the throughput of the KLIP algorithm is accurately taken into account in the disk modeling. To determine the goodness-of-fit of each disk model, we calculate the χ^2 of a rectangular region enclosing the disk, with central pixels close to the star excluded.

The uncertainty per pixel is calculated as a function of radius. We first take the standard deviation of all those pixels outside the mask, in small annuli centered on the star. We then inflate these errors to account for the correlation between pixels. The inflation term is the square root of the number of pixels per correlated region, and is calculated from both the FWHM of the instrument and the radial elongation of speckles due to the filter width (see Figure 1). At radius r, the inflated error is $\sigma(r) = \sqrt{\text{FWHM} \times \text{r}\Delta\lambda/\lambda} \times \sigma_{\text{pixel}}(r)$, where λ and $\Delta\lambda$ are the central wavelength and bandpass of the NIRC2 K' filter. Using this method we find an initial fit value for the first epoch of data using a downhill minimization algorithm. We then initiate Metropolis Hastings MCMC chains from this

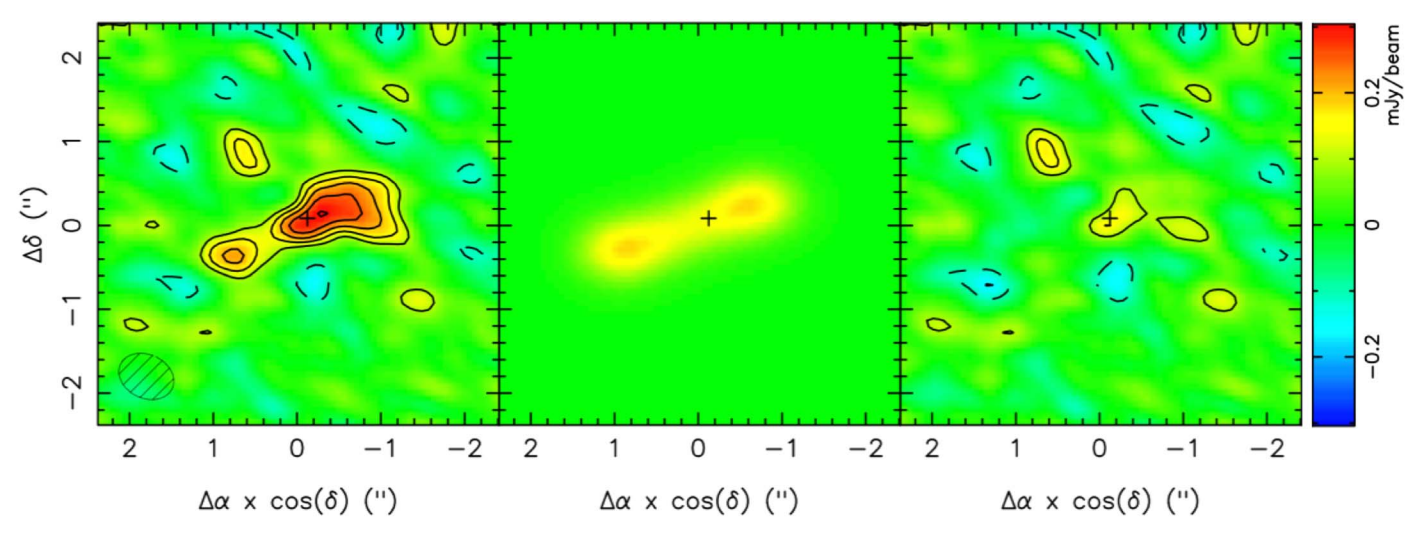


Figure 3. Left: NOEMA CLEAN map of the structure around BD+45° 598. Middle: best-fit model of the disk adjusted to the map as described in Section 3.2. Right: residual map when the model has been subtracted from the CLEAN map. The contours range from $-3, -2, +2, +3 \dots 6\sigma$ in intervals of 1σ , where σ is 42μ Jy/beam. The color coded scale at the right is in units of mJy beam⁻¹, and the beam size is $0\rlap.{''}68 \times 0\rlap.{''}52$. The cross in the map corresponds to the position of the star given in Section 2.3.

initial value to explore the parameter space, and calculate the best fit and uncertainty values. MCMC chains are generated with emcee (Foreman-Mackey et al. 2013), probabilities are assigned to each sample as $\exp{(-\chi^2/2)}$, and we use uniform priors.

We find good fits to each of the three epochs, with the parameters showing good agreement between epochs. Images of the three best-fit models are shown in Figure 2 and best-fit parameters are listed in Table 2, where we list the median and uncertainties, which include 34% of the samples on each side of this median value. The disk is \sim 3° from edge on, and has a radius of \sim 70 au, although the radius is poorly constrained due to the viewing geometry. Given the relatively low signal-to-noise ratio of the disk, we are not able to detect additional structure with the current data.

3.2. IRAM NOEMA Imaging at 1.3 mm

As the Keck scattered light data and the IRAM NOEMA 1.3 mm data are sensitive to dust populations at different radii, we have chosen to model the Keck and NOEMA data separately, and not to perform a simultaneous fit. We have modeled the NOEMA image with the thermal emission of an optically thin ring and again use a Markov Chain Monte Carlo (MCMC) approach using emcee (Foreman-Mackey et al. 2013). The fitting is done by generating disk images, which are then convolved with the NOEMA beam, and then subtracted from the data to create a residual map (from which we compute a χ^2 value). With this approach, the NOEMA radius is constrained to $0.85^{+0.18}_{-0.25}$ (62^{+13}_{-18} au) comparable to the Kuiper Belt radius, the inclination is $87^{\circ+0.46}_{-0.45}$ and the PA is $109.85^{\circ+0.11}_{-0.09}$. The belt radius derived from the NOEMA data is smaller than that derived from the Keck scattered light imaging $(r_0 \sim 70 \text{ au in Table 2})$ as expected since scattered light imaging will be sensitive to micron-sized grains that are likely blown to high eccentricity orbits by radiation pressure, while the NOEMA data set will reveal millimeter-sized grains tracing the belt of larger planetesimals. Higher dynamic range maps would be needed for a detailed comparison of the NOEMA radius with the radius parameter r_0 of the grain surface density in the GRaTeR model used to fit the scattered

 Table 2

 Best-fit Model Parameters to Our K' Scattered Light Data

	2013 Sep 25	2014 Oct 2	2015 Jan 10
PA [°]	$109.9^{+0.6}_{-0.7}$	109.5 ^{+0.9} _{-1.0}	110.2 ± 1.2
$i_{\mathrm{tilt}} \ [^{\circ}]$	$86.9^{+3.0}_{-1.6}$	$87.1^{+3.2}_{-1.7}$	$86.1^{+2.2}_{-2.0}$
$ ho_0$	$1.0^{+0.9}_{-0.4}$	$0.7^{+1.0}_{-0.3}$	$0.9^{+0.7}_{-0.4}$
r_0 [au]	71^{+19}_{-17}	70^{+16}_{-27}	68^{+20}_{-11}
g	$0.44^{+0.32}_{-0.23}$	$0.28^{+0.43}_{-0.17}$	$0.33^{+0.36}_{-0.16}$

Note. ρ_0 values are quoted relative to the first epoch.

light image. Lastly, with the current data, we cannot place strong limits on the belt width besides our constraint that it must be less that 35 au based on FWHM argument mentioned in Section 2.3.

3.3. SED Modeling of BD+45° 598

To construct the SED shown in Figure 4, we collected optical (Tycho-2, APASS, Gaia) and infrared (2MASS, AKARI, WISE, IRAS) photometry for BD+45° 598. We fit the SED with various models, using PHOENIX spectra for the stellar photosphere (Hauschildt et al. 1997), and amorphous silicate spectra for the dust opacity (Li & Greenberg 1997). The silicate models use three parameters; a size distribution $n(D) \propto D^{2-3\,q}$ with a minimum size $D_{\rm min}$, a temperature that corresponds to the blackbody equilibrium temperature $T_{\rm bb}$ at the assumed stellocentric distance, and a normalization parameter (e.g., mass, area, or fractional luminosity). These models are fitted using multinest (Feroz et al. 2009) as described in Yelverton & Kennedy (2018), and also using MCMC using emcee.

We fit two models, both of which have the same stellar component and assume the same silicate optical properties. The first is a theoretical model, in which the dust size distribution is fixed to q=11/6, the minimum grain size to $D_{\min}=1.2~\mu\text{m}$, and the dust blackbody temperature to 40 K (as expected at 62 au, the best-fit parent belt location from modeling the NOEMA data). The only parameter for the dust component in this model is the normalization, and it should fit the data if

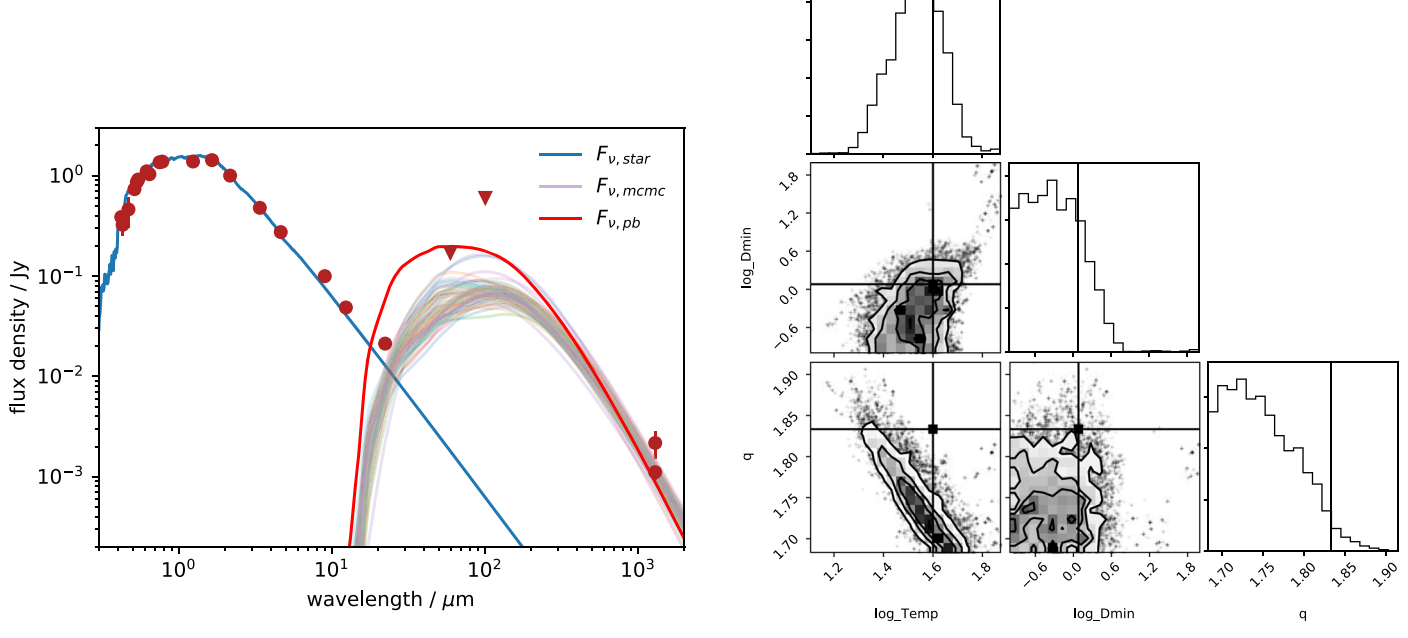


Figure 4. Left: flux density distribution for BD+45° 598, showing observed photometry (filled circles). The blue line denoted by $F_{\nu,star}$ shows the 5280 K stellar model, and the theoretical model of the disk parent belt based on the NOEMA flux density is shown by the red line ($F_{\nu,pb}$). The MCMC best fits of the silicate model are shown by the semitransparent lines. Right: the posterior distributions of the silicate belt parameters with the MCMC chains (crosses are parameter values for the theoretically expected model).

these fairly standard assumptions are correct. The second model is the same, but parameters are allowed to vary.

The best-fit stellar model in both cases has an effective temperature of $5280 \pm 100 \,\mathrm{K}$, consistent with our analysis in Section 4. The luminosity is $L_* = 1.4L_{\odot}$, for which the blowout grain size is 1.2 μ m. The dust models are shown in Figure 4; the red line shows the theoretical model given the parent belt location as imaged by NOEMA $(F_{\nu,pb})$, while the semitransparent lines show a handful of dust models from MCMC fitting that are consistent with the data ($F_{\nu,\text{mcmc}}$). The posterior distributions of the silicate belt parameters are shown in Figure 4, which also shows the parameters of the theoretically expected model. The theoretical model is inconsistent with the posterior distributions for the fitted model, whose size distribution slope is significantly shallower. This discrepancy is caused by the NOEMA flux density being higher than predicted given the mid-IR excess seen with WISE; this pushes the fitted models toward shallower size distributions, whose behavior can be understood in terms of the models presented by Kennedy & Wyatt (2014), e.g., Figure 11 in that work.

The astrosilicate model used here therefore illustrates that there may be a discrepancy between the mid-IR and millimeterwave data, in terms of our ability to explain both with a dust population at a single stellocentric radius. This might be resolved with deeper millimeter-wave imaging to better locate the belt; a more distant location (i.e., a cooler $T_{\rm bb}$) would allow a steeper size distribution to fit the data (Figure 4). Alternatively, the dust spectrum may not come from a single location, for example, comprising both warm inner dust as well as cool outer dust. Nonetheless, we use our fitted model of the infrared excess to calculate a fractional luminosity of $L_{\rm IR}/L_{\rm tot}=6^{+2}_{-1}\times~10^{-4}$, higher than that of the debris disk around AU Mic ($L_{\rm IR}/L_{\rm tot}\simeq 3.5\times 10^{-4}$; Matthews et al. 2015).

3.4. Sensitivity to Low-mass Companions

No significant evidence for point sources that may be selfluminous, massive companions to BD+45° 598 was found within our Keck scattered light images. To assess the sensitivity of our near-infrared coronagraphic observations to substellar companions in the vicinity of BD+45° 598, we start with the angular measure of our achieved 5σ contrast relative to the host star (i.e., a contrast curve). Here we present the contrast performance for only the 2013 September 25 epoch, as this data set delivered the best constraints on planetary mass companions that might be dynamically interacting with the disk. We then use this measure of our 5σ contrast, together with the models of Phillips et al. (2020) assuming an age of 23 ± 3 Myr for the BPMG, to calculate the lower mass limit of substellar objects that would be detectable with our observations described in Section 2.1. Figure 5 shows this sensitivity to substellar companions as a function of projected orbital separation from the host star. Figure 5 also shows a detection probability map (right panel) based on our estimated contrast curve, and generated using the Exo-DMC algorithm (Bonavita 2020), demonstrating that our observations are sensitive to $\sim 8 \, M_{\rm Jup}$ objects at 50 au, and $\sim 3 \, M_{\rm Jup}$ objects at ~ 100 au. In the left panel of Figure 5, we also indicate the upper and lower estimates of the age of the BPMG (27 and 21 Myr, respectively); however, these different ages do not substantially change our overall sensitivity.

4. Age of BD+45° 598

BD+45° 598 was first characterized in a spectroscopic survey of ROSAT All-Sky Survey (RASS) X-ray sources by Guillout et al. (2009). Of the \sim 1000 ROSAT sources studied in that work, BD+45° 598 had the third highest equivalent width of Li I λ 6707.8 (EW \simeq 300.8 \pm 11.6 mÅ), which is above the upper envelope of values seen for Pleiades members.

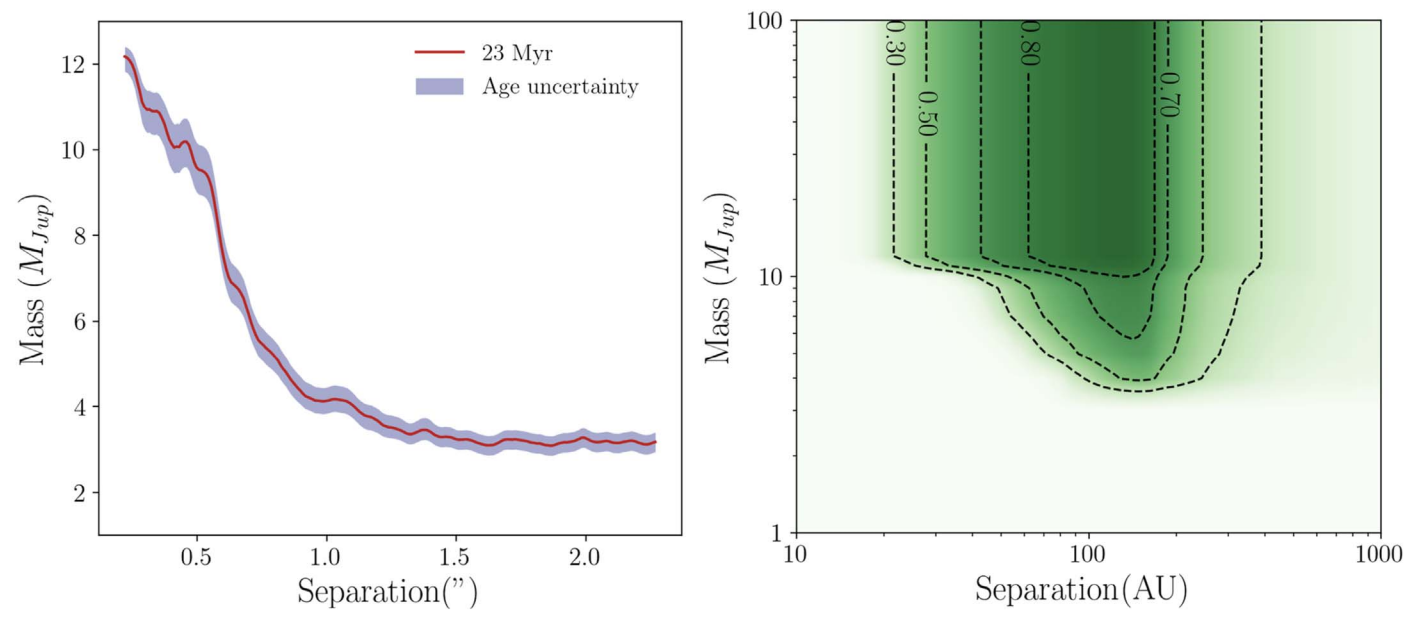


Figure 5. Left: our measured K'-band scattered light contrast limit expressed as the lowest achievable mass (in Jupiter masses) vs. orbital separation in au using the evolutionary models of Phillips et al. (2020). To bound our contrast limit, we also incorporate the upper and lower estimates of the age of the BPMG (27 and 21 Myr, respectively). Right: a probability map for the detection of planetary mass companions calculated using Exo-DMC (Bonavita 2020) using the best estimate age of 23 Myr.

Independent of any other considerations, this observation constrains the star's age to empirically be \lesssim 100 Myr (e.g., Luhman et al. 2005). Kiraga & Stępień (2013) report that the star exhibits saturated X-ray emission, $\log(L_{\rm X}/L_{\rm bol}) = -3.36 \pm 0.14$, and its ASAS photometry shows that the star is a relatively fast rotator (4.73 day period) with strong *V*-band variability (amplitude \simeq 0.07 mag).

Moór et al. (2011) claimed that BD+45° 598 is comoving with the star HD 15745, another star with a debris disk imaged in scattered light (Kalas et al. 2007) situated 9° away, and they further argue based on kinematics and youth indicators that both stars are likely to be members of the BPMG. The median age of the BPMG is now constrained to <15% accuracy $(23 \pm 3 \text{ Myr,Mamajek \& Bell 2014; Bell et al. 2015})$. Binks et al. (2020) used the Gaia Collaboration (2018) astrometry and an adopted radial velocity of $v_R = -1.191 \pm 1.045 \text{ km s}^{-1}$ to estimate a Galactic velocity for BD+45° 598 of U, V, $W = -10.52, -17.32, -9.04 \quad (\pm 0.77, \pm 0.67, \pm 0.26) \quad \text{km s}^{-1}.$ Using the Bayesian classification tool BANYAN Σ , as well as the velocity and position centroids of Gagné et al. (2018), these authors also remark that BD+45° 598 is closest to that of BPMG, the 32 Ori group, and the ϵ Cha group. Binks et al. (2020) notes that the membership probability is highest (yet still meager: 0.3%) for BPMG, providing further support for the membership assignment of Moór et al. (2011). We adopt the new Gaia EDR3 astrometry (Gaia Collaboration et al. 2021) and an updated average radial velocity²⁵ of $v_R = -0.8 \pm 0.3$ km s⁻¹, and estimate an updated velocity of U, V, W = -10.8, $-17.0, -9.2 \ (\pm 0.2, \pm 0.2, \pm 0.2) \ \text{km s}^{-1}$. In Figure 6 we show the U, V, W galactic space velocity for BD+ 45° 598 compared with the representations of several young moving groups taken from Malo et al. (2014) and Weinberger et al. (2013), showing that in all three projections, the Galactic space velocity of BD $+45^{\circ}$ 598 is consistent with membership to the BPMG.

However, running the revised astrometry and radial velocity through the BANYAN Σ kinematic membership tool of Gagné et al. (2018) results in an updated membership probability of 0.2% to BPMG and 99.8% to field (with no other groups breaking above 0.1%).

The reasons for the relatively low probability of membership to the BPMG returned by BANYAN Σ for BD+45° 598 are clear, and primarily stem from its galactic position. Current models of the spatial/kinematic distribution of the BPMG have been primarily constructed using stars within \sim 20–50 pc (e.g., Zuckerman et al. 2001). Therefore, when presented with a target like BD+45° 598 at \sim 73 pc, tools such as BANYAN Σ , will automatically assign a lower membership probability. Indeed, more distant stars like BD+45° 598 that also show multiple clear signs of youth may be essential for extending the model of BPMG members to greater distances. Additionally, the star lies only $\sim 14^{\circ}$ above the galactic plane and has relatively small proper motion, which substantially increases the chances of it being assigned as an interloper to any association by such tools. However, the numerous pieces of evidence pointing to the youth of this star discussed above essentially rule out any chances of being an interloper.

The measured parallax of BD+45° 598 from Gaia means that an HR diagram analysis can be performed to analyze the potential membership to the BPMG. When we compare the $G-K_s$ versus M_G color-magnitude data for the BPMG members in the survey by Binks et al. (2020), we find that BD+45° 598 ($G-K_s=1.68$, $M_G=4.40$) appears right on the single-star trend for BPMG members (approximately $M_G=1.13+1.968(G-K_s)$, for $1.5 < G-K_s < 4.0$). For the $G-K_s$ color of BD+45° 598, one would expect a typical BPMG member to have $M_G \simeq 4.44$, remarkably within 0.04 mag of that observed for the star. Thus, we agree with the assessment of Moór et al. (2011), finding that the proper motion of BD+45° 598, radial velocity, color-magnitude diagram position, presence of lithium, and X-ray emission,

²⁵ Unweighted mean of reported radial velocities from Guillout et al. (2009), Moór et al. (2011), Gaia Collaboration (2018), and this study.

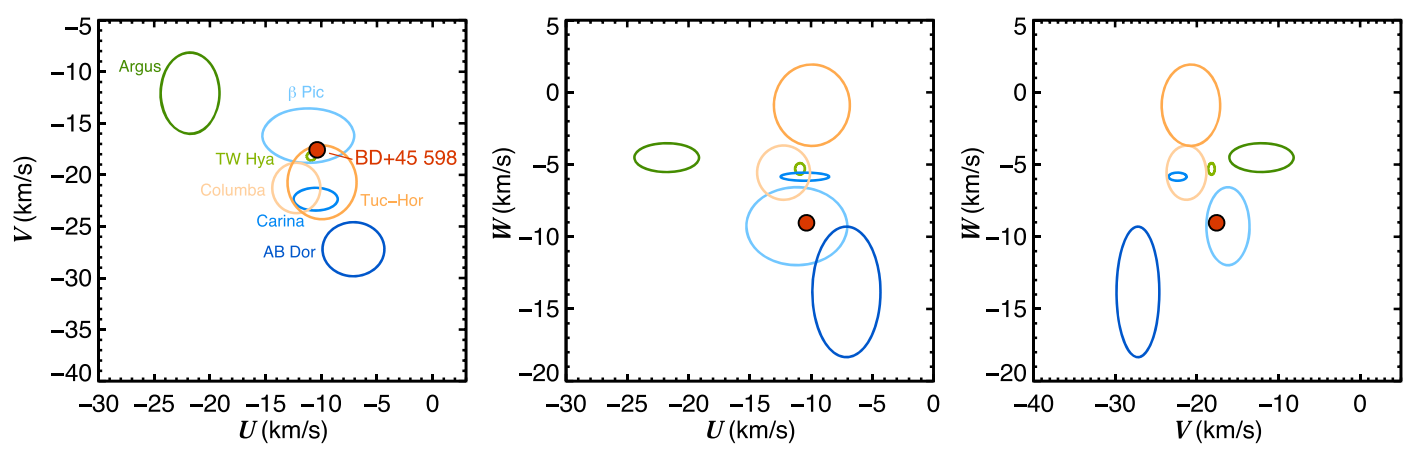


Figure 6. The galactic space velocity representation for several nearby young moving groups (ellipses), as defined from Malo et al. (2014), except for TW Hya taken from Weinberger et al. (2013). The position of BD+45° 598 in this space is shown by the red point, and in all three projections is consistent with membership to the BPMG.

all seem to be consistent with membership of the star to the BPMG.

5. Summary and Conclusions

We have identified a nearly edge-on circumstellar debris disk, imaged in scattered light at the W.M. Keck Observatory, associated with the nearby K1 star BD+45° 598. We have shown that this star's proper motion, radial velocity, colormagnitude diagram position, presence of lithium, and X-ray emission, are all consistent with membership in the BPMG with age 23 ± 3 Myr. Using the NOEMA interferometer at the Plateau de Bure Observatory operating at 1.3 mm, we also find a 4σ – 5σ detection of a source aligned with the orientation of the disk structure in the 2.2 μ m images. Our best-fitting model to the disk scattered light images is one with a peak disk radius at ~70 au, and a fractional luminosity $L_{\rm IR}/L_{\rm tot} \simeq 6^{+2}_{-1} \times 10^{-4}$. Recently Moór et al. (2020) and Tanner et al. (2020) presented the discovery of CP-72 2713, another BPMG member with a cold debris disk, and a relatively high fractional luminosity of 1.1×10^{-3} , suggesting it is a more massive, dust-rich "sibling" to the debris disk system associated with AU Mic $(L_{\rm IR}/L_{\rm tot} \simeq 3.5 \times 10^{-4}; \text{ Matthews et al. 2015}).$ With a fractional luminosity of $L_{\rm IR}/L_{\rm tot} \simeq 6^{+2}_{-1} \times 10^{-4}, \text{ our study suggests}$ BD+45° 598 could also be considered another dust-rich counterpart to AU Mic. However, some differences between AU Mic and BD+45° 598 are apparent. Namely, previous studies of AU Mic using the SMA and ALMA find a central radius for the emission belt of 35-40 au (Wilner et al. 2012; MacGregor et al. 2013), while our observations find a significantly larger radius of \sim 70 au.

Systems like BD+45° 598 and CP-72 2713 may be examples of newly identified late-type members of YMGs that provide an opportunity to study the evolution of debris disks starting at the earliest ages. Discovery of more such systems would complement previous infrared and millimeter surveys for debris disks within nearby young moving groups (e.g Rebull et al. 2008; Donaldson et al. 2012; Riviere-Marichalar et al. 2014; Moór et al. 2016; Binks & Jeffries 2017; Holland et al. 2017). While the youngest associations of stars have been efficient at producing scattered light systems (e.g., Sco-Cen, Esposito et al. 2020), debris structures in nearby YMGs span a range of ages from ~10 to 100 Myr, which will allow us to image in sequence the evolution of circumstellar environments

after the era of massive planet formation has ceased. Thus, with its young age of ~ 20 Myr, and reasonably close proximity (~ 70 pc), BD+45° 598 will be an excellent target for upcoming high-contrast imaging missions in the northern hemisphere (e.g., Chilcote et al. 2018; Currie et al. 2020), to search for massive companions at close orbital separations (~ 5 –20 au), or possibly even much-lower-mass companions at wider orbital separations (20–200 au) using the upcoming James Webb Space Telescope (Hinkley et al. 2018; Carter et al. 2021).

We thank the anonymous referee for several helpful comments, which improved the quality of the manuscript. Some of this work was performed in part under an NSF Astronomy and Astrophysics Postdoctoral Fellowship under award AST-1203023. Some of the data presented herein were obtained at the W.M. Keck Observatory, which is operated as a scientific partnership among the California Institute of Technology, the University of California and NASA. The Observatory was made possible by the generous financial support of the W.M. Keck Foundation. The authors wish to recognize and acknowledge the very significant cultural role and reverence that the summit of Maunakea has always had within the indigenous Hawaiian community. Part of this work has been carried out within the framework of the National Centre of Competence in Research PlanetS supported by the Swiss National Science Foundation. E.C.M. acknowledges the financial support of the SNSF. G.M.K. is supported by the Royal Society as a Royal Society University Research Fellow. The Submillimeter Array is a joint project between the Smithsonian Astrophysical Observatory and the Academia Sinica Institute of Astronomy and Astrophysics and is funded by the Smithsonian Institution and the Academia Sinica. This work used the Immersion Grating Infrared Spectrometer (IGRINS) that was developed under a collaboration between the University of Texas at Austin and the Korea Astronomy and Space Science Institute (KASI) with the financial support of the Mt. Cuba Astronomical Foundation, of the US National Science Foundation under grants AST-1229522 and AST-1702267, of the McDonald Observatory of the University of Texas at Austin, of the Korean GMT Project of KASI, and Gemini Observatory. This paper includes data taken at The McDonald Observatory of The University of Texas at Austin. Part of this research was carried out at the Jet Propulsion Laboratory, California Institute of Technology, under a

contract with the National Aeronautics and Space Administration (80NM0018D0004).

ORCID iDs

Sasha Hinkley https://orcid.org/0000-0001-8074-2562 Elisabeth C. Matthews https://orcid.org/0000-0003-0593-1560 Charlène Lefevre https://orcid.org/0000-0001-7349-6113 Grant Kennedy https://orcid.org/0000-0001-6831-7547 Dimitri Mawet https://orcid.org/0000-0002-8895-4735 Karl R. Stapelfeldt https://orcid.org/0000-0002-2805-7338 Eric Mamajek https://orcid.org/0000-0003-2008-1488 Brendan P. Bowler https://orcid.org/0000-0003-2649-2288 David Wilner https://orcid.org/0000-0003-1526-7587 Jonathan Williams https://orcid.org/0000-0001-5058-695X Mark Wyatt https://orcid.org/0000-0001-9064-5598 Mark W. Phillips https://orcid.org/0000-0001-6041-7092 Ben J. Sutlieff https://orcid.org/0000-0002-9962-132X Brenda Matthews https://orcid.org/0000-0003-3017-9577 Henry Ngo https://orcid.org/0000-0001-5172-4859 Justin R. Crepp https://orcid.org/0000-0003-0800-0593 Andrew W. Mann https://orcid.org/0000-0003-3654-1602 Gregory Mace https://orcid.org/0000-0001-7875-6391

- Grorod, P. A. 1999, A&A, 348, 557 Mouillet, D. 2001, A&A, 370, 447 ApJL, 278, L23 Backman, D. E., & Paresce, F. 1991, Metic, 26, 314 Bell, C. P. M., Mamajek, E. E., & Naylor, T. 2015, MNRAS, 454, 593 Binks, A. S., & Jeffries, R. D. 2017, MNRAS, 469, 579 Binks, A. S., Jeffries, R. D., & Wright, N. J. 2020, MNRAS, 494, 2429 Astrophysics Source Code Library, ascl:2010.008 A&A, 597, L7 877, 60 Stapelfeldt, K. R. 2009, ApJ, 705, 1226
- Hillenbrand, L. A. 2009, ApJS, 181, 197 Carter, A. L., Hinkley, S., & Bonavita, M. 2021, MNRAS, 501, 1999 Proc. SPIE, 10702, 1070244 Cotten, T. H., & Song, I. 2016, ApJS, 225, 15 Currie, T., Guyon, O., Lozi, J., et al. 2020, Proc. SPIE, 11448, 114487H Dominik, C., & Decin, G. 2003, ApJ, 598, 626 2012, ApJ, 753, 147 555, A11 Duchene, G. 2020, arXiv:2004.13722

```
References
Augereau, J. C., Lagrange, A. M., Mouillet, D., Papaloizou, J. C. B., &
Augereau, J. C., Nelson, R. P., Lagrange, A. M., Papaloizou, J. C. B., &
Aumann, H. H., Gillett, F. C., Beichman, C. A., DeJong, T., & Houck 1984,
Bonavita, M. 2020, Exo-DMC: Exoplanet Detection Map Calculator, v1,
Bonnefoy, M., Milli, J., Ménard, F., Vigan, A., & Lagrange, A. M. 2017,
Bowler, B. P., Hinkley, S., Ziegler, C., Baranec, C., & Gizis, J. E. 2019, ApJ,
Bryden, G., Beichman, C. A., Carpenter, J. M., Rieke, G. H., &
Carpenter, J. M., Bouwman, J., Mamajek, E. E., Meyer, M. R., &
Chiang, E., Kite, E., Kalas, P., Graham, J. R., & Clampin, M. 2009, ApJ,
Chilcote, J. K., Bailey, V. P., De Rosa, R., Macintosh, B., & Nielsen, E. 2018,
Donaldson, J. K., Roberge, A., Chen, C. H., Augereau, J. C., & Dent, W. R. F.
Eiroa, C., Marshall, J. P., Mora, A., Montesinos, B., & Absil, O. 2013, A&A,
Esposito, T. M., Kalas, P., Fitzgerald, M. P., Millar-Blanchaer, M. A., &
Feroz, F., Hobson, M. P., & Bridges, M. 2009, MNRAS, 398, 1601
Foreman-Mackey, D., Hogg, D. W., Lang, D., & Goodman, J. 2013, PASP,
Gagné, J., & Faherty, J. K. 2018, ApJ, 862, 138
Gagné, J., Mamajek, E. E., Malo, L., Riedel, A., & Rodriguez, D. 2018, ApJ,
   856, 23
Gaia Collaboration 2018, yCat, 1345, 0
Gaia Collaboration, Brown, A. G. A., Vallenari, A., et al. 2021, A&A, 649, A1
Gaia Collaboration, Brown, A. G. A., Vallenari, A., Prusti, T., &
   de Bruijne, J. H. J. 2018, A&A, 616, A1
```

```
Hinkley et al.
Guillout, P., Klutsch, A., Frasca, A., Freire Ferrero, R., & Marilli, E. 2009,
  A&A, 504, 829
Hauschildt, P. H., Baron, E., & Allard, F. 1997, ApJ, 483, 390
Hillenbrand, L. A., Carpenter, J. M., Kim, J. S., Meyer, M. R., &
  Backman, D. E. 2008, ApJ, 677, 630
Hinkley, S., Carter, A., Biller, B., & Skemer, A. 2018, EPSC, 12,
  EPSC2018-923
Hinkley, S., Oppenheimer, B. R., Soummer, R., Sivaramakrishnan, A., &
  Roberts, L. C., Jr. 2007, ApJ, 654, 633
Högbom, J. A. 1974, A&AS, 15, 417
Holland, W. S., Matthews, B. C., Kennedy, G. M., Greaves, J. S., &
  Wyatt, M. C. 2017, MNRAS, 470, 3606
Hughes, A. M., Duchêne, G., & Matthews, B. C. 2018, ARA&A, 56, 541
Janson, M., Brandt, T. D., Moro-Martín, A., Usuda, T., & Thalmann, C. 2013,
   ApJ, 773, 73
Kalas, P., Duchene, G., Fitzgerald, M. P., & Graham, J. R. 2007, ApJL,
  671, L161
Kennedy, G. M., & Wyatt, M. C. 2014, MNRAS, 444, 3164
Kenyon, S. J., & Bromley, B. C. 2004, AJ, 127, 513
Kenyon, S. J., & Bromley, B. C. 2008, ApJS, 179, 451
Kiraga, M., & Stępień, K. 2013, AcA, 63, 53
Kraus, A. L., Shkolnik, E. L., Allers, K. N., & Liu, M. C. 2014, AJ, 147, 146
Launhardt, R., Henning, T., Quirrenbach, A., Ségransan, D., & Avenhaus, H.
  2020, A&A, 635, A162
Li, A., & Greenberg, J. M. 1997, A&A, 323, 566
Lindegren, L. 2020, A&A, 633, A1
Lindegren, L., Bastian, U., & Biermann, E. A. 2021, A&A, 649, A4
Luhman, K. L., Stauffer, J. R., & Mamajek, E. E. 2005, ApJL, 628, L69
MacGregor, M. A., Wilner, D. J., Rosenfeld, K. A., Andrews, S. M., &
  Matthews, B. 2013, ApJ, 762, L21
Malo, L., Doyon, R., Feiden, G. A., Albert, L., & Lafrenière, D. 2014, ApJ,
Mamajek, E. E., & Bell, C. P. M. 2014, MNRAS, 445, 2169
Marois, C., Lafrenière, D., Doyon, R., Macintosh, B., & Nadeau, D. 2006, ApJ,
  641, 556
Matthews, B. C., Kennedy, G., Sibthorpe, B., Holland, W., & Booth, M. 2015,
   ApJ, 811, 100
Matthews, B. C., Krivov, A. V., Wyatt, M. C., Bryden, G., & Eiroa, C. 2014, in
  Protostars and Planets VI, ed. H. Beuther et al. (Tucson, AZ: Univ. Arizona
  Press), 521
Matthews, B. C., Sibthorpe, B., Kennedy, G., Phillips, N., & Churcher, L.
  2010, A&A, 518, L135
Matthews, E., Hinkley, S., Vigan, A., Kennedy, G., & Rizzuto, A. 2017, ApJL,
  843, L12
Matthews, E., Hinkley, S., Vigan, A., Kennedy, G., & Sutlieff, B. 2018,
   MNRAS, 480, 2757
Meshkat, T., Mawet, D., Bryan, M. L., Hinkley, S., & Bowler, B. P. 2017, AJ,
  154, 245
Moór, A., Kóspál, Á, Ábrahám, P., Balog, Z., & Csengeri, T. 2016, ApJ,
```

Rebull, L. M., Stapelfeldt, K. R., Werner, M. W., Mannings, V. G., & Chen, C.

Rieke, G. H., Su, K. Y. L., Stansberry, J. A., Trilling, D., & Bryden, G. 2005,

Moór, A., Pascucci, I., Kóspál, Á, Ábrahám, P., & Csengeri, T. 2011, ApJS,

826, 123

&A, 553, A60

2008, ApJ, 681, 1484

ApJ, 620, 1010

- Riviere-Marichalar, P., Barrado, D., Montesinos, B., Duchêne, G., & Bouy, H. 2014, A&A, 565, A68
- Sibthorpe, B., Kennedy, G. M., Wyatt, M. C., Lestrade, J. F., & Greaves, J. S. 2018, MNRAS, 475, 3046
- Silverberg, S. M., Kuchner, M. J., Wisniewski, J. P., & Bans, A. S. 2018, ApJ, 868, 43
- Smith, B. A., & Terrile, R. J. 1984, Sci, 226, 1421
- Soummer, R., Pueyo, L., & Larkin, J. 2012, ApJL, 755, L28
- Su, K. Y. L., Rieke, G. H., Malhotra, R., Stapelfeldt, K. R., & Hughes, A. M. 2013, ApJ, 763, 118
- Tanner, A., Plavchan, P., Bryden, G., Kennedy, G., & Matrá, L. 2020, PASP, 132, 084401
- Torres, C. A. O., Quast, G. R., da Silva, L., de La Reza, R., & Melo, C. H. F. 2006, A&A, 460, 695

- Trilling, D. E., Bryden, G., Beichman, C. A., Rieke, G. H., & Su, K. Y. L. 2008, ApJ, 674, 1086
- Wahhaj, Z., Liu, M. C., Biller, B. A., Nielsen, E. L., & Hayward, T. L. 2014, A&A, 567, A34
- Weinberger, A. J., Anglada-Escudé, G., & Boss, A. P. 2013, ApJ, 762, 118
- Wilner, D. J., Andrews, S. M., MacGregor, M. A., & Hughes, A. M. 2012, ApJL, 749, L27
- Wizinowich, P., Acton, D. S., Shelton, C., Stomski, P., & Gathright, J. 2000, PASP, 112, 315
- Wyatt, M. C. 2003, ApJ, 598, 1321 Wyatt, M. C. 2005, A&A, 440, 937
- Wyatt, M. C. 2008, ARA&A, 46, 339
- Wyatt, M. C., & Dent, W. R. F. 2002, MNRAS, 334, 589
- Yelverton, B., & Kennedy, G. M. 2018, MNRAS, 479, 2673
- Zuckerman, B., Song, I., Bessell, M. S., & Webb, R. A. 2001, ApJL, 562, L87